Russian Journal of Earth Sciences

Reconstruction of the Angular Dependence of the Sea Ice Backscattering Pattern According to the GNSS-R Data

D. Kovaldov[1,*], V. Karaev[1], Yu. Titchenko[1], V. Fateev[2], V. Lopatin[2], F. Huang[3], X. Wang[4], and J. Guo[4]

[1] Institute of Applied Physics, Russian Academy of Sciences, Nizhny Novgorod, Russia
[2] All-Russian Scientific Research Institute for Physical-Engineering and Radiotechnical Metrology (VNIIFTRI), Mendeleyevo, Moscow Region, Russia
[3] National Space Science Center, Chinese Academy of Sciences (NSSC/CAS), Beijing, China
[4] CAS Key Laboratory of Coastal Environmental Processes and Ecological Remediation, Yantai Institute of Coastal Zone Research, Chinese Academy of Sciences, Yantai, China
* **Correspondence to:** Dmitriy Kovaldov, dmit.kovaldov@gmail.com

Abstract: This study addresses the challenge of understanding sea ice microwave scattering properties by developing a novel method to retrieve scattering indicatrix and angular dependence of backscattering patterns from Global Navigation Satellite System Reflectometry (GNSS-R) data. Sea ice remote sensing in quasi-specular reflection area requires theoretical models validated using experimental data across different frequency bands. However, only limited observations of quasi-specular scattering in the L-band exist. We developed an algorithm to convert Doppler spectra from delay-Doppler maps (DDM) obtained by the TDS-1 satellite into scattering indicatrix and then to angular dependence of the sea ice backscattering patterns, using geometric transformations from bistatic sensing geometry. The method was applied to approximately 100 DDM measurements over the Sea of Okhotsk during February–March 2017, where ice concentration remained at 90–100% with temperatures below 0 °C. Results show that L-band (19 cm wavelength) exhibits broader angular dependence compared to Ka-band (8.45 mm) and Ku-band (2.21 cm) measurements from dual-frequency precipitation radar (DPR), contrary to expectations based solely on surface roughness. This anomalous broadening is attributed to volume scattering effects within sea ice, where L-band signals penetrate up to one meter depth compared to millimeter-scale penetration in Ka- and Ku-frequency bands. The findings provide new insights into L-band scattering mechanisms and offer a validated approach for improving theoretical models of sea ice microwave interaction.

Keywords: bistatic, scattering indicatrix, angular dependence of backscattering, sea ice, remote sensing, L-band, GPS, TDS-1, GNSS-R.

Citation: Kovaldov D., Karaev V., Titchenko Yu., Fateev V., Lopatin V., Huang F., Wang X., and Guo J. (2025), Reconstruction of the Angular Dependence of the Sea Ice Backscattering Pattern According to the GNSS-R Data, *Russian Journal of Earth Sciences*, 25, ES5022, EDN: WQDUDV, https://doi.org/10.2205/2025es001082

Research Article

Received: September 16, 2025
Accepted: November 6, 2025
Published: December 1, 2025

1. Introduction

Microwave remote sensing methods are used to study the sea and ocean ice in a variety of scientific and practical areas [*Vagapov et al.*, 1993]. These methods are particularly used to study the interaction of sea waves with ice cover [*Mitnik and Viktorov*, 1990], to create ice maps for planning shipping routes [*Smith et al.*, 2019], and to analyze climate changes affecting the ice cover area [*Mitnik and Kalmykov*, 1992] and the physical properties of ice [*Sandven et al.*, 2023]. Qualitative interpretation of remote sensing results requires theoretical approaches to be developed and numerical models to be created to simulate the scattering of microwave signals by different types of reflective surfaces. In the field of sea waves, several microwave scattering models have been developed, which are based on statistical wave parameters such as significant wave height, mean square slope, or orbital velocity variance of the sea surface [*Bass and Fuks*, 1979; *Karaev et al.*, 2020; *Titchenko*, 2020;

Zapevalov and Knyazkov, 2019]. These statistical parameters are calculated using wave spectrum models [*Elfouhaily et al.*, 1997; *Hwang and Fois*, 2015; *Kudryavtsev et al.*, 1999; *Ryabkova et al.*, 2019]. An alternative approach uses wave correlation functions instead of statistical characteristics [*Voronovich*, 1994; *Voronovich and Zavorotny*, 2001]. Analysis of slope variance distribution across different wave scales for quasi-specular reflection applications is presented in [*Zapevalov and Knyazkov*, 2019]. However, validating such models is difficult since, unlike statistical parameters, correlation functions cannot be directly measured experimentally.

Theoretical analysis and mathematical modeling of ice cover are significantly more complex than those of the water surface [*Golden et al.*, 1998; *Lebedev and Sukhorukov*, 2001]. The process of ice formation creates a multi-level, stratified structure that significantly impacts the propagation and scattering of microwave radiation within the ice layer. Air bubbles and brine cells are inhomogeneously distributed within the ice cover volume. Additionally, the penetration depth of microwave radiation (the skin depth) varies depending on the wavelength of the signal and is determined by the temperature and salinity conditions of the ice [*Winebrenner et al.*, 1992]. Consequently, various components can contribute to the formation of the reflected microwave signal, including the upper boundary between ice and the atmosphere, the lower boundary between ice and water (typical for freshwater ice), and the complex internal architecture of the entire ice mass. Consequently, the scattering of microwave radiation by an ice cover is a multi-parameter problem, with parameters that are difficult to regulate or measure remotely over vast territories [*Fil'chuk et al.*, 2023]. This creates significant difficulties when comparing experimental data with the results of numerical modeling.

The reflective properties of ice cover in the microwave range are determined using a monostatic remote sensing scheme, in which the transmitter and receiver can be considered to be located at the same point. The result of using such a sensing scheme is the dependence of the backscattering radar cross section on the incidence angle. In the range of moderate incidence angles, similar dependencies for ice cover are determined using data from synthetic aperture radars (SAR) and scatterometers [*Dadjoo et al.*, 2024; *Geldsetzer and Howell*, 2023; *Onstott*, 1992]. With the accumulation of a sufficient amount of experimental data based on the obtained dependencies, empirical models are created [*Komarov and Buehner*, 2019; *Mahmud et al.*, 2018] and theoretical concepts are verified [*Komarov et al.*, 2015]. Currently, interest in studying the reflective properties of ice cover in the range of small incidence angles (near-nadir range) has significantly increased [*Freilich and Vanhoff*, 2003; *Hauser et al.*, 2017; *JAXA*, 2014]. Using dual-frequency precipitation radar (DPR) data, an empirical reflection model was developed for Ku-band incidence angles up to 18 degrees and Ka-band incidence angles up to 9 degrees and compared with existing theoretical models for the specified range of incidence angles [*Karaev et al.*, 2021].

More than half a century ago, the idea of using reflected signals from satellite systems for remote sensing of the earth's surface using bistatic methods was put forward [*Sutton et al.*, 1973]. When recording reflected signals from global navigation satellite systems (GNSS-R), the configuration of the measuring system is bistatic, but the nature of the scattering scheme remains quasi-specular, similar to the case of a monostatic DPR radar.

Currently, global navigation satellite systems (GNSS) include GLONASS (Russia), BeiDou (China), GPS (USA), and Galileo (Europe). Within the framework of the proposed concept, a GNSS transmitting element combined with a receiving device capable of analyzing reflected GNSS signals forms a bistatic remote sensing scheme [*Hall and Cordey*, 1988]. The concept of analyzing signals of the satellite navigation system reflected from the water surface was presented in 1993 [*Martín-Neira*, 1993]. The proposal to use reflected radiation from satellite navigation systems to solve a variety of problems was considered a promising direction, which contributed to the rapid development of the theoretical foundations of this approach to remote sensing [*Cardellach et al.*, 2011; *Chernoukhov and Dobykin*, 1995; *Zavorotny et al.*, 2014]. The first experimental work on recording reflected GPS signals from aircraft was carried out in the mid-2000s [*Nogués-Correig et al.*, 2007]. Subsequently,

key studies of L-band signal reflection by the sea surface were carried out using the SMOS (Soil Moisture and Ocean Salinity) and Aquarius space radiometers [*Lagerloef et al.*, 2008; *McMullan et al.*, 2008].

Retrieval of geophysical parameters via GNSS-R relies on analyzing changes in the reflected L-band signal's characteristics, including its waveform, amplitude, phase, frequency, and polarization. The core observables used are the Delay-Doppler Map (DDM), primarily for spaceborne platforms like CYGNSS. For ocean applications, wind speed and sea surface roughness are determined from the DDM's peak value and shape, which reflects the degree of quasi-specular scattering caused by wind-generated waves. Sea surface height (altimetry) is extracted by measuring the time delay between the direct and reflected signals. Over land, parameters like Soil Moisture are linked to the surface's dielectric constant, which dictates signal reflectance, and are derived using techniques such as GNSS-Interferometric Reflectometry (GNSS-IR) based on periodic SNR fluctuations or bistatic radar methods utilizing the DDM to calculate reflectivity. Furthermore, sea ice thickness and snow depth are estimated using altimetric models or phase difference measurements. All these retrievals translate the physical properties of the scattering surface into geophysical outputs using established theoretical models.

Small satellites of the British disaster monitoring mission UK-DMC (United Kingdom – Disaster Monitoring Constellation) [*Gleason et al.*, 2005] from 2004 to 2011 successfully carried out numerous experiments to demonstrate the capabilities of analyzing GPS signals reflected from water, land, and ice cover [*Clarizia et al.*, 2009; *Gleason*, 2006, 2010; *Gleason et al.*, 2009; *Hobiger et al.*, 2014]. Also, GNSS-R methods have been used to determine parameters such as geoid height and deflection of the plumb line [*Lopatin et al.*, 2024; *Lopatin and Fateev*, 2022], sea surface wind speed [*Clarizia et al.*, 2014; *Li and Huang*, 2014], soil moisture [*Alonso Arroyo et al.*, 2014; *Chew et al.*, 2016], and characteristics of vegetation [*Camps et al.*, 2016; *Yang et al.*, 2020], snow [*Larson et al.*, 2009; *Najibi and Jin*, 2013], and ice cover [*Cartwright et al.*, 2019; *Yan and Huang*, 2019].

Depending on the type of the GNSS receiver carrier (stationary, airborne, or spaceborne), the areas of application of this technology and algorithms for processing reflected signals may differ. In the presented work, a method for determining the angular dependence of the backscattering pattern is proposed. The angular dependence of the backscattering pattern is the dependence of the scattered signal power on the incidence angle, determined from the results of bistatic remote sensing. This concept was developed during the work with monostatic radar data, where the dependence of the backscattering radar cross section on the incidence angle was obtained based on the Doppler spectrum of the reflected signal for a radar located on a moving carrier [*Kovaldov et al.*, 2024]. In the case of a bistatic remote sensing scheme, reconstructing the angular dependence of the backscattering pattern involves two steps. First, a transition is made from the Doppler spectrum of the received signal to the scattering indicatrix – the dependence of the scattered signal power on the grazing angles of the reflected radiation for a fixed grazing angle of the transmitter signal. Since the grazing angle of the transmitter signal can change for each measurement, the scattering indicatrix is different for each measurement. To obtain a universal characteristic, a transition is made from the scattering indicatrix to a dependence on half the grazing angle difference. At this stage, a backscattering pattern is obtained – a dependence similar to the dependence of the backscatter cross section on the incidence angle, determined by a monostatic radar. The resulting backscattering pattern is universal, independent of the measurement geometry, and determined only by the characteristics of the scattering surface. The obtained data make it possible to verify theoretical scattering models and advance in the creation of a theoretical scattering model for sea ice in the quasi-specular reflection region in the L-band.

In this study, we used TDS-1 satellite data at a selected testing site in the Sea of Okhotsk with low temperatures for February–March 2017. The choice was based on data from meteorological stations, images from the Aqua satellite (EOS PM-1), ice cover maps from the "Planeta" Research Center, and ice concentration maps from the University of Bremen, which are constructed using data from the AMSR-2 radiometer.

2. Materials and Methods

2.1. Measurement Scheme Using GNSS-R Methods

In this paper, GPS satellites with orbital altitudes of 20 180 km act as transmitters, and the TDS-1 satellite with orbital altitudes of 635 km, acts as a receiver. In this paper, we will limit ourselves to considering the reflected L1 signal (1575.42 MHz). The radiation pattern (RP) of the transmitter is designed in such a way that the signal uniformly illuminates the visible surface of the Earth.

A GPS signal receiver (SGR-ReSI (Space GPS Receiver Remote Sensing Instrument)) with a sampling frequency of 16.367 MHz was installed on board the TDS-1 satellite. The receiver's antenna pattern (radiation pattern, RP) is 34°×35° [*MERRByS*, 2025]. Simplified geometry of bistatic (example of the TDS-1 satellite) remote sensing schemes is shown in Figure 1b. For comparison and visual representation, an example of a monostatic radar remote sensing scheme is also provided in Figure 1a. We can do early assumptions that in both cases the scattering mechanism is quasi-specular. The difference is that in the case of monostatic, a backscattered signal is received, and in the case of bistatic, a forward scattered signal is received.

In the given example of a monostatic measurement scheme by the dual-frequency precipitation radar DPR of the GPM satellite (Figure 1a), the statistical characteristics of the surface are determined by the dependence of the backscattering RCS on the incidence angle.

Figure 1b shows an example of a bistatic remote sensing scheme for the TDS-1 satellite. In this measurement scheme, due to the large difference in the altitudes of the transmitter and receiver orbits, it can be assumed that the incident wave on the reflecting area has a constant grazing angle (flat front). In this case, the way of the rays entering the receiver after reflection from the rough surface is shown in Figure 1b.

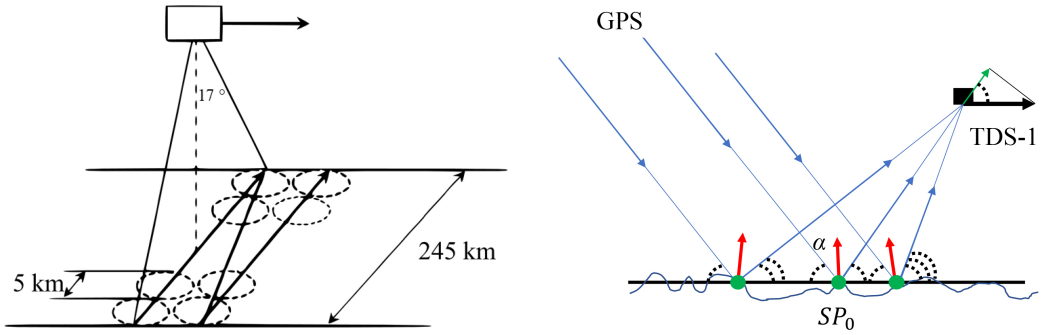

Figure 1. Simplified geometry of: (a) monostatic (example of the GPM mission satellite [*JAXA*, 2014]); and (b) bistatic (example of the TDS-1 satellite) remote sensing schemes.

The reflected signal enters the receiver at different angles. Each angle has its own projection of velocity onto the receiver sensing direction, and therefore its own Doppler shift frequency, which forms the Doppler spectrum. If we perform the inverse procedure and go from the Doppler shift frequencies to the grazing angles, we can obtain a scattering indicatrix. This requires information on the velocities and positions of the transmitter and receiver, the position of the reflection point, and the measured Doppler spectrum.

Although GNSS-R operates in a bistatic configuration measuring forward-scattered signals, the quasi-specular reflection geometry allows us to retrieve scattering characteristics equivalent to monostatic measurements. Through geometric transformation, we convert the bistatic scattering indicatrix to an angular dependence that represents the same physical surface scattering properties as would be measured by a monostatic radar. Therefore, we use the term 'backscattering pattern' to emphasize that the retrieved angular dependence is universal and can be directly compared with monostatic radar measurements and used in monostatic scattering models.

In the case of TDS-1, the main product used to analyze the reflecting surface in such a task is a delay-Doppler map (DDM), which is obtained by Fourier transformation and cross-correlation function of the reflected signal and the simulated signal of the navigation satellite. This procedure is carried out in a special Zoom Transform Correlator (ZTC). Each pixel in the DDM represents the correlation power at a specific delay and Doppler shift. The power values are stored as digital counts (0–65 535), with the scaling factor saved in metadata. These 'raw counts DDM power' values are proportional to the actual received power but require calibration for absolute measurements. In this study, we work with relative power in dB, as we focus on the angular dependence shape rather than absolute scattering cross-sections.

Figure 2 shows a map of sea ice concentration (SIC) with a scale in percentages, where 0% is clear water, 100% is ice in the Weddell Sea in November 2017, and the red line shows the track of the specular points for the TDS-1 satellite. This track contains 2 points: 1 of which relate to the surface with 0% concentration (the sea surface), and 1 relate to the surface with almost 100% concentration (solid ice cover).

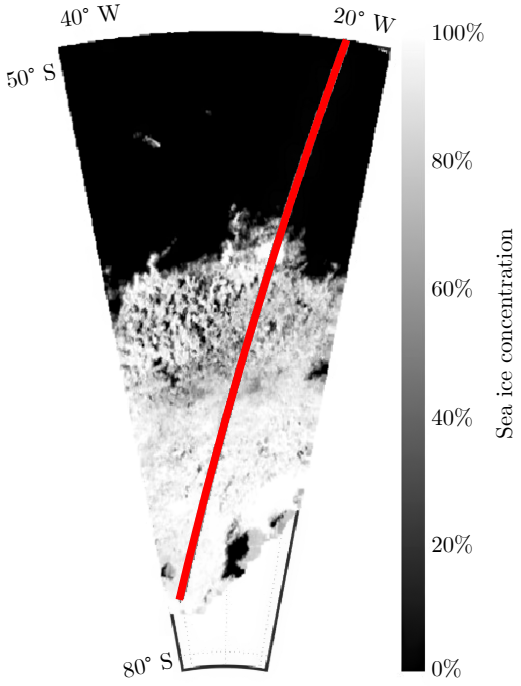

Figure 2. Ice concentration map with TDS-1 specular points (red) plotted on it. Ice concentration is presented as a percentage (0% – clear water, 100% – ice).

Figure 3 shows examples of recorded DDMs when a signal is reflected from different surfaces (ice and water). The differences between them are obvious, and modern studies often use the original DDMs to determine the type of reflecting surface. For this purpose, neural networks are used [*Yan and Huang*, 2018; *Yan et al.*, 2017], or the DDM itself is used as variable and differential characteristics are analyzed [*Zhu et al.*, 2017].

The theoretical Doppler spectrum would exhibit a sinc-like shape due to the GPS signal's ambiguity function. Surface roughness causes scattering from multiple surface facets with different slopes, spreading the energy across a wider Doppler range, thus producing a Doppler spectrum like in the Figure 3 and 5, even for ice cover.

However, despite the effectiveness of DDM-based surface classification methods for determining ice/water surface type, they do not provide information about the scattering properties. To improve ice cover scattering models and validate them, it is necessary to extract the dependence of raw counts DDM power on the incidence angle from DDM data. Therefore, in this paper, we propose a new approach to obtain the angular dependence

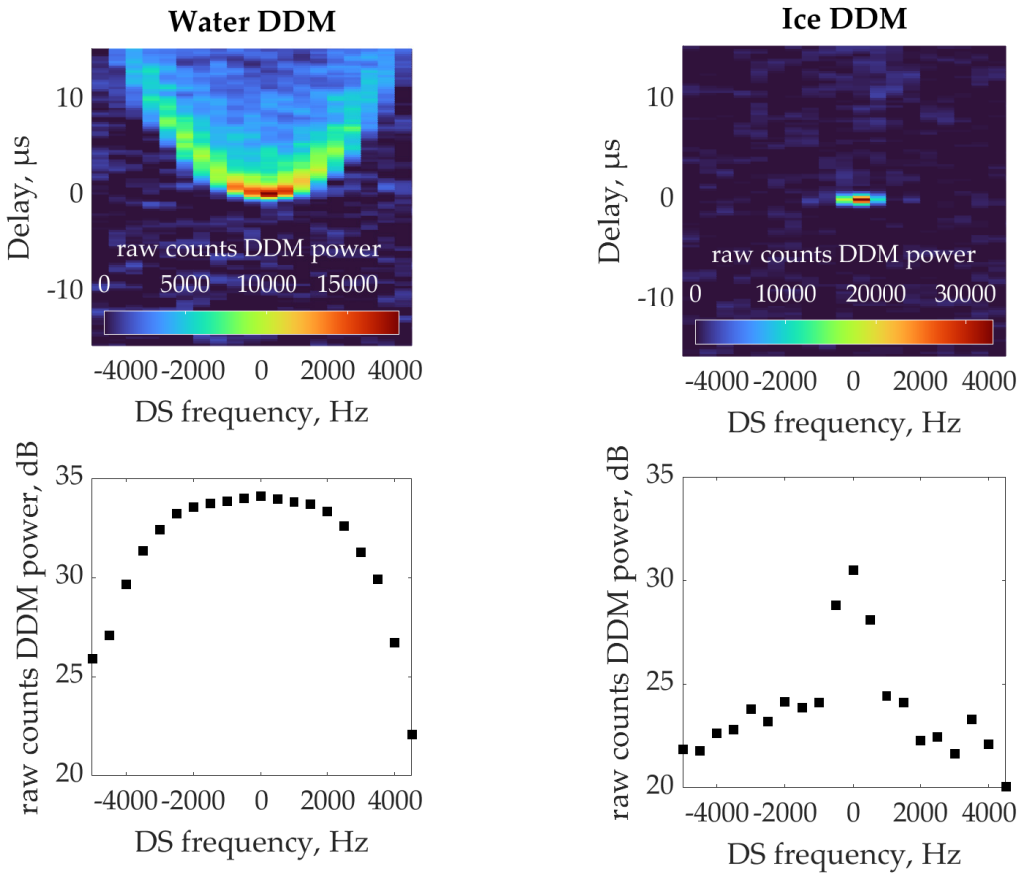

(a) Rough water surface. **(b)** Ice cover.

Figure 3. Normalized DDM and Doppler spectra.

of backscattering pattern from the Doppler spectrum contained in the DDM, which will allow comparison with monostatic radar measurements and theoretical scattering models for ice cover in the L-band.

To obtain the Doppler spectrum of the reflected signal, we first subtract the noise calculated from the first 5 rows of pixels, using such a noise box is standard procedure [*MERRByS*, 2025], and then perform the DDM summation procedure over the whole delay. The corresponding Doppler spectra of the reflected signal are shown at the bottom part of Figure 3.

Several factors affect the obtained Doppler spectra, and in this regard, it is worth making several remarks about the fact that the received signal passes through the ionosphere, and in some cases, it is necessary to consider the influence of the Faraday effect on the measurements conducted. This effect has a significant influence in the case of linearly polarized radiation, as, for example, in radiometric measurements of surface brightness temperature [*Danilychev et al.*, 2018]. The influence of ionospheric plasma on GNSS signals is related to ionospheric plasma inhomogeneity and affects both signal phase and amplitude [*Kintner et al.*, 2007].

The influence of the troposphere is usually divided into two classes: hydrostatic ("dry") delay caused by dry gases present in the troposphere, and wet delay caused by the presence of water vapor and condensed water in the form of clouds.

Thus, regarding GNSS-R methods, the Faraday effect and ionospheric inhomogeneity affect signal phase and amplitude. Signal phase during further processing affects the measurement of range to reflecting patches, but not the frequency distribution of Doppler shifts, which depends only on the projection of the receiver velocity onto the direction of reflected radiation. The influence of the troposphere is also related only to range.

The method considered and applied in this work to obtain the angular dependence of the ice cover backscattering pattern is based on summation over delays and formation of the Doppler spectrum of the reflected signal, which eliminates the influence of phase shift when the microwave signal passes through the ionosphere.

In the case of amplitude, it should be clarified that the geometry for each individual specular point constantly changes, which also has a significant influence on the amplitude of the received signal. In this work, we focus on the form of the angular dependence of the sea ice backscattering pattern. Therefore, at this stage of the research, this effect can also be disregarded. This is an advantage of this approach to data analysis.

2.2. Algorithm for transition from Doppler spectrum to angular dependence

To convert the obtained Doppler spectra into angular dependence:

For the initial modeling of geometry, let us consider a sphere with the radius of the Earth. Through the specular reflection point on the sphere, we will draw a tangent plane. We will call this plane the specular plane.

Based on three points: the position of the transmitter, receiver, and the specular reflection point we construct a reflection plane (Figure 4). The direction of wave propagation (straight lines passing through the positions of the transmitter/receiver and the specular point on the plane) of the transmitter and receiver lie in the reflection plane. The grazing angle for specular point corresponds to 0 in the Doppler spectrum and we call it the central grazing angle. In Figure 4, it is designated as α. For the central grazing angle, in the case of movement parallel to the specular plane, the Doppler shift is written as follows:

$$V_{\tau_0} = v_{\text{tr}} \cdot \cos(\alpha) - v_{\text{rec}} \cdot \cos(\alpha) \Rightarrow f_{\text{DS}_0} = V_{\tau_0}/\lambda_{\text{GPS}},$$

where V_{τ_0} is the sum of velocity projections onto the sensing direction, v_{tr} is the transmitter velocity, v_{rec} is the receiver velocity, α is the grazing angle of the incident and reflected signal, and λ_{GPS} is the GPS wavelength. In general, to determine the projection of the transmitter and receiver velocity vectors onto the corresponding sensing directions, the scalar product between the velocity vectors and the sensing direction vectors is used. The origin of these direction vectors is always placed at the specular point, and the end point corresponds to the position of the respective satellite. Thus, $\cos(\alpha)$ can take negative values, which allows accounting for different signs of the velocity vector directions.

We construct a straight line formed by the intersection of two planes (the specular plane and the reflection plane, the black line in Figure 4), which we call the specular line. It will be used to calculate the dependence of Doppler shift on the grazing angle of the reflected radiation.

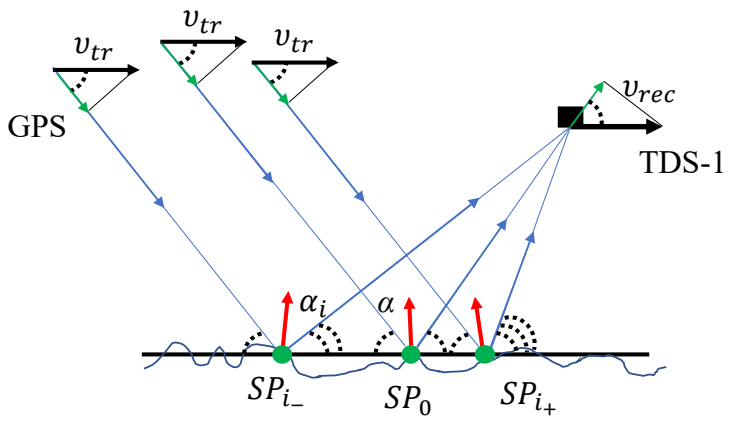

Figure 4. Signal propagation scheme in the reflection plane.

We select several points on the specular line. Since the transmitter signal arrives at the surface with a constant grazing angle α, only the change in reception direction affects the formation of the Doppler spectrum.

For each selected point on the sensing line, we calculate the projection of the receiver velocity onto the reception direction and the grazing angle of the reflected radiation. As an example, Figure 4 shows a point for which this angle corresponds to α_i.

Each point is characterized by its own grazing angle α_i. For each such angle, some correspondence is established with the change in Doppler shift relative to the central one based on the previously calculated projection of the receiver velocity:

$$\begin{aligned}\Delta f_i(\alpha_i) &= f_{\mathrm{DS}_0} - f_i \\ &= \frac{((v_{\mathrm{tr}} \cdot \cos(\alpha) - v_{\mathrm{rec}} \cdot \cos(\alpha)) - (v_{\mathrm{tr}} \cdot \cos(\alpha) - v_{\mathrm{rec}} \cdot \cos(\alpha_i)))}{\lambda_{\mathrm{GPS}}} \\ &= v_{\mathrm{rec}} \frac{\cos(\alpha_i) - \cos(\alpha)}{\lambda_{\mathrm{GPS}}},\end{aligned}$$

where f_i is the Doppler shift when the signal is reflected from the i-th specular point, and f_{DS_0} is the Doppler shift when the signal is reflected from the central specular point. Thus, the transition from the Doppler spectrum of the reflected signal to the scattering indicatrix is accomplished. This characteristic depends on the central grazing angle; for comparison with monostatic dependence, we will transition to surface slope. We consider only points along the specular line, as this simplifies the geometry and allows us to account for the main contribution of scattering. In reality, this is used only to convert Doppler shift frequencies into surface deflection angles.

We make the transition from the scattering indicatrix to the dependence of raw counts DDM power on the incidence angle θ_i. To derive Equation 1, we use the relationship between grazing angles and incidence angles. In the bistatic configuration, the incidence angle θ_i can be used as half the angular deviation from the specular direction when the transmitter grazing angle remains constant:

$$\theta_i(\Delta f_i) = \frac{(\alpha_i(\Delta f_i) - \alpha)}{2}. \tag{1}$$

It is important to note that θ_i represents the surface slope angle relative to the surface normal, not the actual incidence angle of the electromagnetic wave. This is consistent with the monostatic radar interpretation where, for near-nadir observations, the measured backscatter at angle θ corresponds to surface facets tilted by θ from horizontal. This interpretation allows direct comparison with monostatic measurements where the same surface slope angles contribute to the received signal. The disadvantage of this approach is that the points on the specular line are selected sequentially with a constant step. This leads to an uneven step along the Doppler spectrum. To eliminate the unevenness of the step, an approximation of the obtained dependence of the frequency shift on the incidence angle by a fifth-degree polynomial is used. It should be noted that the points are selected in such a way that the obtained frequency limits are always greater than the real spectra (> 4500 Hz and < -5000 Hz) to avoid incorrect approximation at the ends of the dependence. Figure 5 shows the sequential transformation: DDM $\Rightarrow$ DS $\Rightarrow$ scattering indicatrix $\Rightarrow$ angular dependence of backscattering pattern.

2.3. Characteristics of the marine testing site

To reconstruct the angular dependence of the sea ice backscattering pattern in the L-band using GNSS-R methods, it is necessary to select a site with ice cover (marine test site) who's SIC during measurements remains at the level of 90–100% and the air temperature should not rise above 0 °C. This allows avoiding cases of wet/moist snow and water film formation on the ice surface. In this case, it can be considered that reflection occurred from

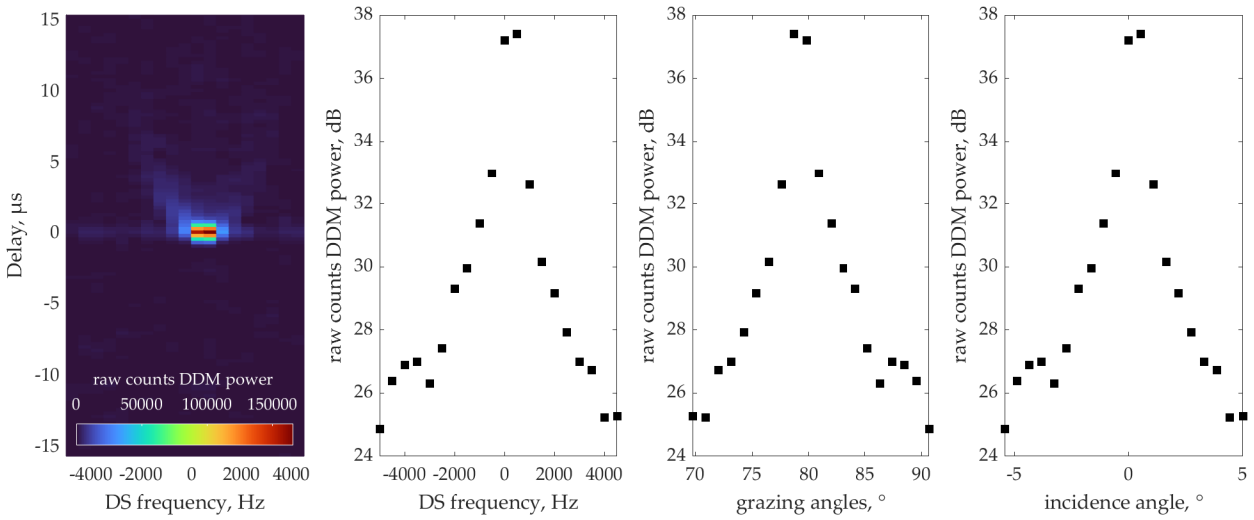

Figure 5. Sequential transformation: DDM ⇒ DS ⇒ scattering indicatrix ⇒ angular dependence of backscattering pattern.

"dry" ice. There are limitations on the choice of year, determined by the operational period of TDS-1 (2014–2018), so 2017 was selected for analysis.

The Sea of Okhotsk waters north of Sakhalin Island and covering the entire coastal zone of the Khabarovsk region were considered. In this area, there are meteorological stations Okha, located on Sakhalin Island, and Bolshoy Shantar, located on the Shantar Islands. To select the time frame, air temperature data from January 1 to April 1, 2017 were used (https://rp5.ru/). Figure 6a shows the air temperature dependence according to meteorological station data and the geographical location of the meteorological stations on the map (Figure 6b). Thus, the time interval from February to March 2017 was chosen, when the air temperature was below zero.

As already indicated, it is necessary that throughout the entire period, the test site had ice cover with high concentration. To determine this characteristic, concentration maps constructed from University of Bremen data were used [*Melsheimer and Spreen*, 2019].

For subsequent analysis, the coordinates of the rectangle within this site were specified (corner coordinates: 53°30' N, 135°0' E, 55°30' N, 135°0' E, 55°30' N, 142°30' E, 53°30' N, 142°30' E). The average SIC in this site during the observation period (February–March) was approximately 95% – solid ice (Figure 7).

To clarify information about the ice cover condition, maps from the Research Center "Planeta" (http://planet.iitp.ru) were used (Figure 8, left and right symbol descriptions). According to the maps, the total ice cover concentration was 10 points ("Planeta" scale) in the observed site, that is, solid ice, or 100% in terms of University of Bremen data.

According to the maps of March 7 and 21, the characteristics of the ice cover in the selected site remained unchanged. The overall ice cover concentration reached 10 points, with the ice being represented mainly by ice fields of first-year dry, medium, and thin ice. The process of ice cover growth with a gradual increase in the total area was noted. In this regard, this region is optimal for measuring the angular dependence of the sea ice backscattering pattern in the L-band and for conducting a comparative analysis with the dependence of the RCS on incidence angle in the Ka- and Ku-bands.

3. Results

In the first stage of processing, points located in the Sea of Okhotsk waters during February–March 2017 were selected. As a result, approximately 10 000 DDM measurements were obtained over the entire Sea of Okhotsk. Some records were corrupted due to reception instability. Such DDMs were filtered out based on the difference between peak power and DDM noise level. After conducting the filtering procedure and limiting

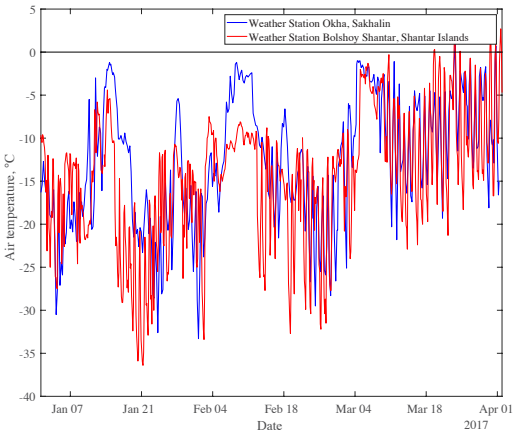

(a) Temperature change from January 1 to April 1, 2017. Data from the Okha weather station is blue, data from the Bolshoy Shantar weather station is in red.

(b) The locations of the weather stations on the map are shown on the right.

Figure 6. Data from ground weather stations (https://rp5.ru/).

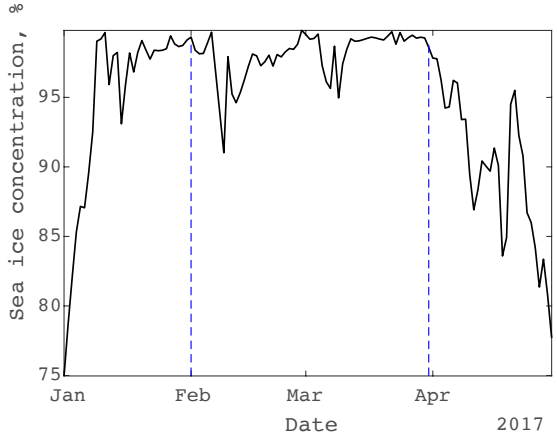

Figure 7. Average SIC in the selected site from January 1 to April 30, 2017; blue dashed lines mark the observation boundaries used in this work.

the observation site to the specified rectangle (Figure 9b, red rectangle), approximately 100 points remained for further analysis. According to Research Center "Planeta" data, the ice cover consisted of ice fields of first-year dry medium (70–120 cm) and thin ice (30–70 cm).

Figure 9a shows an example of DDM during stable signal reception and the corresponding Doppler spectrum.

For comparison with previous studies with monostatic radar, an empirical model for the dependence of backscatter RCS on the angle of incidence was proposed. Based on data from the DPR installed on the GPM mission satellite, an empirical model was constructed [*Karaev et al.*, 2022a,b]. We adapt this model first for the grazing angles, which can be used for modeling bistatically scattered signal, and then for the incidence angles, for comparison with monostatic data:

$$F(\alpha) = a + b \cdot \left|\frac{(\alpha - \alpha_0)}{2}\right| + c \cdot \left(\frac{(\alpha - \alpha_0)}{2}\right)^2 + d \cdot \exp\left(-e\left|\frac{(\alpha - \alpha_0)}{2}\right|\right),$$
$$F(\theta) = a + b \cdot \theta + c \cdot \theta^2 + d \cdot exp(-e|\theta|), \quad (2)$$

where a, b, c, d, e are coefficients that are fitted, α is the grazing angle, α_0 is the grazing angle at the specular point, and θ is the incidence angle. The approximation of experimental

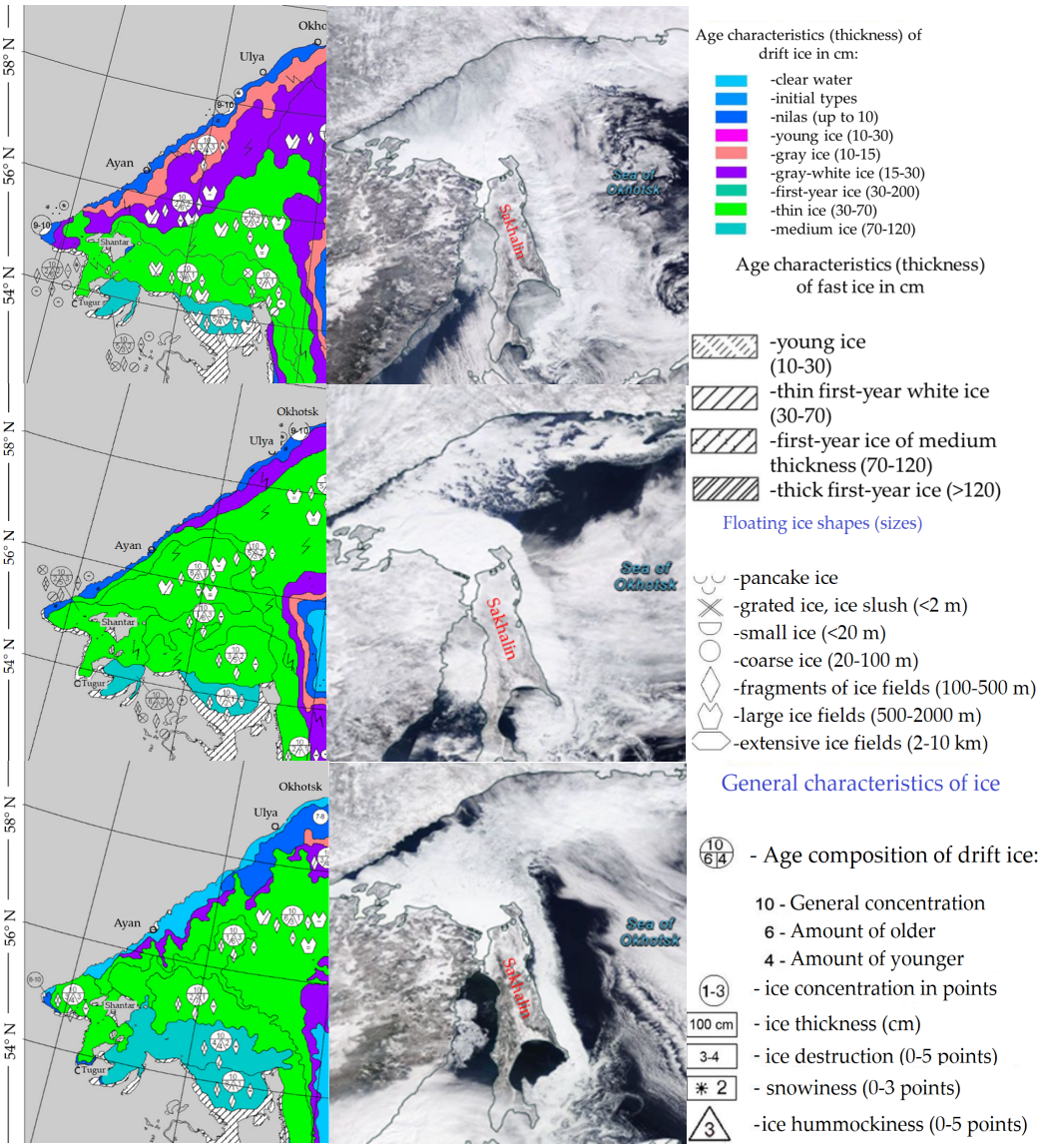

Figure 8. Ice cover maps of the Sea of Okhotsk (Research Center "Planeta", http://planet.iitp.ru) (left) and optical images of the Sea of Okhotsk (center) and symbols with descriptions for ice cover maps (right).

angular dependences of backscattering pattern in the L-band is shown in Figure 10a, and the approximation coefficients are given in the table in Figure 10b. Figure 10 shows the angular dependence for surface slope angles up to 7°. These small angles correspond to the quasi-specular reflection region.

Let us consider the DPR data for the same time interval. Figure 11 shows radar images in the test site on March 13, 2017, for the Ku- and Ka-bands.

Figure 12a shows the measured RCS for March 13, 2017, for the Ku- and Ka-bands, and the curves show approximations (2) obtained from these data. The coefficient table is provided in the figure. To compare the decay rate of the dependencies, the approximation curves in the L-, Ku-, and Ka-bands were aligned at an incidence angle of 1° (Figure 12b).

The approximation for the Ku-band turned out narrower than the approximation in the Ka-band, which indicates "greater" surface roughness in the Ka-band than in the Ku-band. However, the approximation of the angular dependence of backscattering pattern in the L-band turned out to be the broadest. It was expected that this characteristic would

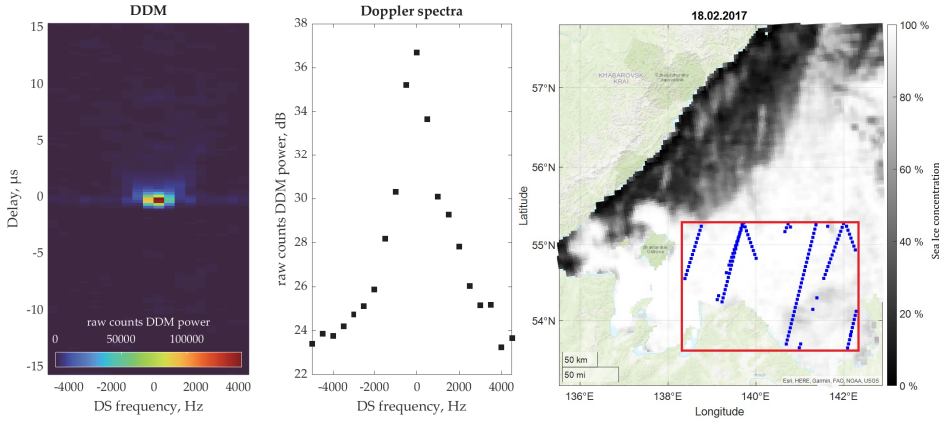

(a) Example of DDM and Doppler spectrum in the considered site.

(b) SIC map from February 18, 2017, with specular reflection points from February to March that fell within the selected site for analysis plotted on it.

Figure 9. Data from test site.

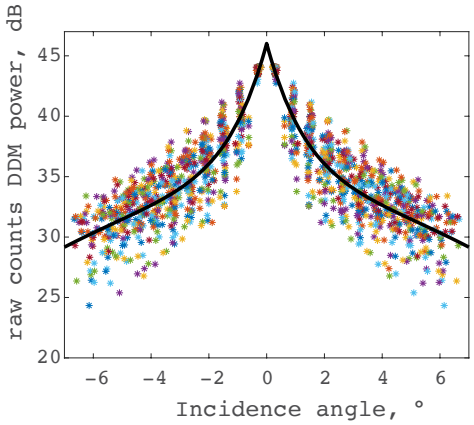

a	33.15 ± 0.45
b	≈ 0.00
c	-0.0834 ± 0.0126
d	12.86 ± 0.37
e	0.690 ± 0.057

(a) **(b)**

Figure 10. The angular dependence of backscattering pattern of sea ice (dots) in the L-band and approximation curve (black curve), approximation coefficients are shown in the figure in the table.

be the narrowest if the influence factor of roughness remained the most significant. We assume that this is related to the influence of volume scattering.

For the Ka- and Ku-bands, the skin depth for sea ice is about several millimeters [*Winebrenner et al.*, 1992]: for Ka −0.0073 m, for Ku −0.0040 m. For the L-band, the skin depth can vary within much larger limits from decimeters to several meters Figure 13, since the L-band is sensitive to sea ice salinity [*Timchenko et al.*, 1985]. The comparison with DPR data is valid because both GNSS-R and DPR sensing the same surface slope distribution in the quasi-specular regime. While the measurement geometries differ (bistatic vs monostatic), both techniques are sensitive to surface facets with slopes that redirect the incident signal toward the receiver. The retrieved angular dependencies therefore represent the same statistical distribution of surface slopes.

For example, for electromagnetic radiation with a frequency of 1.5 GHz at a sea ice salinity of 5.1‰ and temperature of −20 °C, the skin depth is about 1 m. Thus, the main parameter on which signal scattering depends in the Ka- and Ku-bands is the distribution of reflectors at the interface between two media due to rapid attenuation inside sea ice in these bands. Meanwhile, electromagnetic radiation in the L-band experiences additional influence from multiple reflections within the medium and scattering on inclusions.

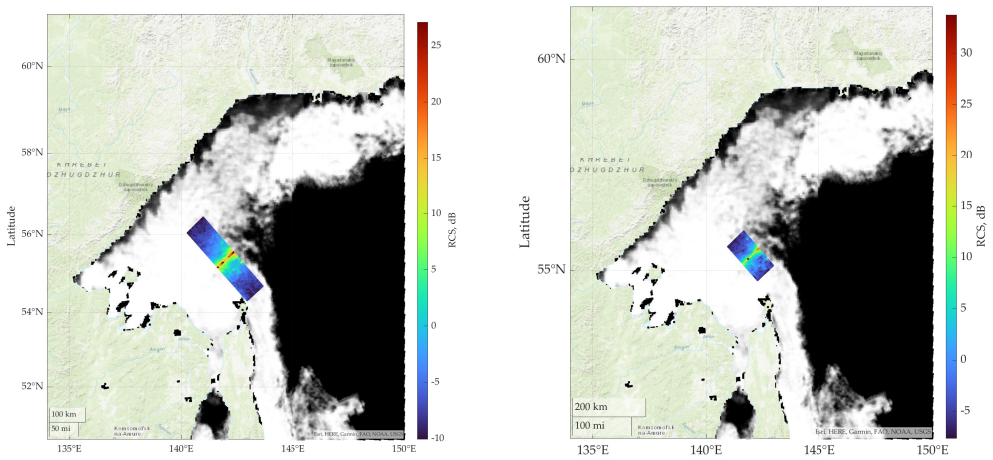

(a) Ku-band. **(b)** Ka-band.

Figure 11. SIC map from March 13, 2017, with plotted DPR track segments.

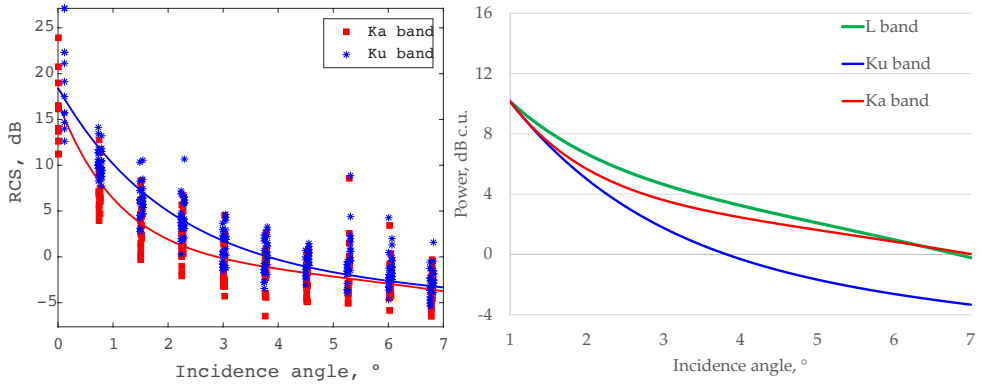

(a) Experimental points and approximation of DPR data in the Ka- and Ku-bands.

(b) Comparison of approximations in the L-, Ku-, and Ka-bands normalized to the same value at 1° incidence angle.

Figure 12. Backscatter approximations across multiple frequency bands.

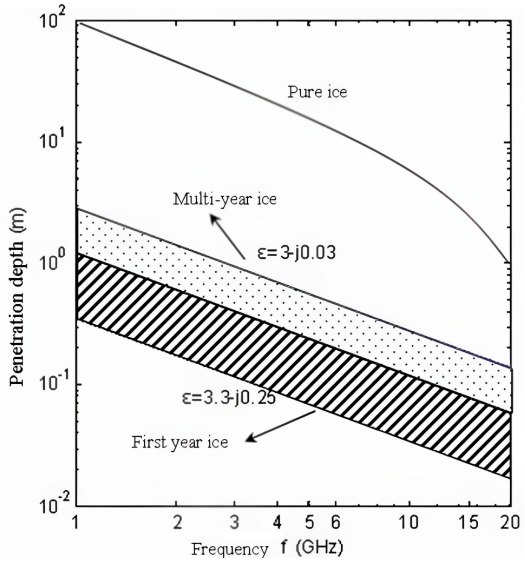

Figure 13. Experimental penetration depth for sea ice [*Ulaby et al.*, 1986].

4. Discussion

4.1. Characteristics of Incidence Angle Dependence in Different Frequency Bands

The obtained results revealed significant differences in the angular dependence of backscattering pattern between measurements conducted using GNSS-R methods in the L-band and data taken from the dual-frequency DPR radar in the Ku- and Ka-bands. The angular dependence of backscattering pattern in the L-band demonstrates the broadest dependence among all analyzed frequency bands, which contradicts the expected behavior based solely on surface roughness considerations.

In the Ka-band (8.45 mm), the dependence of backscattering cross-section on incidence angle is broader than in the Ku-band (2.21 cm), which corresponds to theoretical expectations [*Karaev et al.*, 2021], since shorter wavelengths are more sensitive to surface roughness distribution. However, the similar dependence in the L-band (20 cm) shows unexpected broadening despite the longer wavelength, which we associate with volume scattering.

4.2. Volume Scattering Effects in Sea Ice

The anomalous broadening of the angular dependence of backscattering pattern in the L-band can be explained by volume scattering effects within the sea ice medium. The skin depth varies dramatically across different frequency bands: in the Ka- and Ku-bands it is fractions of millimeters, indicating predominantly reflection at the ice-water boundary. In the L-band, the skin depth varies strongly depending on medium parameters (salinity and temperature). For example, for sea ice with salinity of 5.1‰ at temperature −20 °C, the penetration depth can reach 1 meter.

This substantial difference in penetration depth indicates that while Ka- and Ku-band signals mainly interact with the air-ice interface, L-band signals penetrate deep into the ice structure, scattering on internal inclusions such as brine cells, air bubbles, and layered structures formed during ice formation. The contribution of volume scattering in the L-band effectively increases the apparent "roughness" of the scattering medium, leading to broadening of the dependence.

4.3. Algorithm for Converting Doppler Spectra to Incidence Angle Dependence

The developed algorithm allows transformation of Doppler spectra obtained from bistatic sensing data into the angular dependence of the sea ice backscattering pattern, providing a new approach for investigating sea ice cover properties in various bands. The quasi-specular scattering mechanism in the GNSS-R method indicates that the obtained angular dependence of the sea ice backscattering pattern has a similar nature to dependencies obtained in monostatic sensing, which will allow further improvement of ice cover scattering models and their extension to L-band.

4.4. Data Quality and Limitations

The study analyzed approximately 100 DDMs over the selected test site in the Sea of Okhotsk during February–March 2017, obtained from TDS-1 satellite data [*Hallikainen and Winebrenner*, 1992]. We deliberately chose the simplest constant ice conditions and limited our consideration to a single winter season. The results obtained do not cover all the variability of sea ice conditions, and the results are for first-year sea ice in the Sea of Okhotsk region and may not be directly applicable to other ice types or geographic locations. Further research will also be directed toward determining patterns in seasonal processes and in other water bodies.

5. Conclusions

In this study, a new approach to studying the reflection of microwave signal by sea ice is discussed, based on the use of Doppler spectra obtained by GNSS-R methods. In this work, an original algorithm for converting Doppler spectra into scattering indicatrix and angular dependencies of backscattering pattern is developed.

The universal nature of the retrieved angular dependence enables several applications: direct validation of theoretical ice scattering models without geometric transformation, cross-calibration between different remote sensing systems operating in quasi-specular geometry and development of unified scattering models applicable to both monostatic and bistatic configurations.

An important result of the study is a comparison of the angular dependencies of backscattering pattern and dependences of backscatter RCS for three wavelength bands: Ku-, Ka-, and L-bands. It was shown that the L-band exhibits broadening of the angular dependence compared to the Ku- and Ka-bands. This may be due to greater skin depth in the L-band, where the internal structure of the ice cover affects the result. The greater signal penetration depth in the L-band provides sensitivity to the volumetric characteristics of the ice cover. The obtained results will improve and validate theoretical models of microwave signal scattering by ice cover.

It should be noted that this study was limited to analyzing data from a single winter season in a limited geographic region and focused on first-year sea ice. Future studies will aim to include multi-year data covering different ice types and geographic regions.

Acknowledgments. The research was supported by Russian Science Foundation (RSF) project No. 23-67-10007, https://rscf.ru/project/23-67-10007/. The authors express their gratitude to A. Maksimov and R. Volgotov from the "Planeta" Research Center for preparing the data for analysis.

References

Alonso Arroyo A., Camps A., Aguasca A., et al. Dual-Polarization GNSS-R Interference Pattern Technique for Soil Moisture Mapping // IEEE Journal of Selected Topics in Applied Earth Observations and Remote Sensing. — 2014. — Vol. 7, no. 5. — P. 1533–1544. — https://doi.org/10.1109/JSTARS.2014.2320792.

Bass F. G. and Fuks I. M. Wave Scattering from Statistically Rough Surfaces. — New York : Elsevier, 1979. — https://doi.org/10.1016/c2013-0-05724-6.

Camps A., Park H., Pablos M., et al. Sensitivity of GNSS-R Spaceborne Observations to Soil Moisture and Vegetation // IEEE Journal of Selected Topics in Applied Earth Observations and Remote Sensing. — 2016. — Vol. 9, no. 10. — P. 4730–4742. — https://doi.org/10.1109/jstars.2016.2588467.

Cardellach E., Fabra F., Nogués-Correig O., et al. GNSS-R ground-based and airborne campaigns for ocean, land, ice, and snow techniques: Application to the GOLD-RTR data sets // Radio Science. — 2011. — Vol. 46, no. 6. — RS0C04. — https://doi.org/10.1029/2011RS004683.

Cartwright J., Banks C. J. and Srokosz M. Sea Ice Detection Using GNSS-R Data From TechDemoSat-1 // Journal of Geophysical Research: Oceans. — 2019. — Vol. 124, no. 8. — P. 5801–5810. — https://doi.org/10.1029/2019jc015327.

Chernoukhov V. V. and Dobykin V. D. Scattering of electromagnetic waves by the sea surface at two-position location // Radiotehnika i Elektronika. — 1995. — Vol. 40, no. 3. — P. 464–471. — (In Russian).

Chew C., Shah R., Zuffada C., et al. Demonstrating soil moisture remote sensing with observations from the UK TechDemoSat-1 satellite mission // Geophysical Research Letters. — 2016. — Vol. 43, no. 7. — P. 3317–3324. — https://doi.org/10.1002/2016GL068189.

Clarizia M. P., Gommenginger C. P., Gleason S. T., et al. Analysis of GNSS-R delay-Doppler maps from the UK-DMC satellite over the ocean // Geophysical Research Letters. — 2009. — Vol. 36, no. 2. — P. L02608. — https://doi.org/10.1029/2008GL036292.

Clarizia M. P., Ruf C. S., Jales P., et al. Spaceborne GNSS-R Minimum Variance Wind Speed Estimator // IEEE Transactions on Geoscience and Remote Sensing. — 2014. — Vol. 52, no. 11. — P. 6829–6843. — https://doi.org/10.1109/tgrs.2014.2303831.

Dadjoo M., Mayvan M. Z. and Isleifson D. Experimental Observations of Forming Sea Ice Using Surface-Based L-, C-, and Ku-Band Polarimetric Scatterometers // IGARSS 2024 - 2024 IEEE International Geoscience and Remote Sensing Symposium. — IEEE, 2024. — P. 76–79. — https://doi.org/10.1109/igarss53475.2024.10640527.

Danilychev M. V., Kutuza B. G., Moshkov A. V., et al. The application of L-band in satellite microwave radiometry of the sea surface // Physical Bases of Instrumentation. — 2018. — Vol. 7, no. 1. — P. 46–53. — https://doi.org/10.25210/jfop-1801-046053. — (In Russian).

Elfouhaily T., Chapron B., Katsaros K., et al. A unified directional spectrum for long and short wind-driven waves // Journal of Geophysical Research: Oceans. — 1997. — Vol. 102, no. C7. — P. 15781–15796. — https://doi.org/10.1029/97jc00467.

Fil'chuk K. V., Kovalev S. M., Guzenko R. B., et al. Ice research in the expedition "North Pole-41" // Rossijskie polârnye issledovaniâ. — 2023. — 3 (53). — P. 19–28. — EDN: IGTWSQ ; (in Russian).

Freilich M. H. and Vanhoff B. A. The Relationship between Winds, Surface Roughness, and Radar Backscatter at Low Incidence Angles from TRMM Precipitation Radar Measurements // Journal of Atmospheric and Oceanic Technology. — 2003. — Vol. 20, no. 4. — P. 549–562. — https://doi.org/10.1175/1520-0426(2003)20<549:trbwsr>2.0.co;2.

Geldsetzer T. and Howell S. E. L. Incidence Angle Dependencies for C-Band Backscatter From Sea Ice During Both the Winter and Melt Season // IEEE Transactions on Geoscience and Remote Sensing. — 2023. — Vol. 61. — P. 1–15. — https://doi.org/10.1109/tgrs.2023.3315056.

Gleason S. Remote Sensing of Ocean, Ice and Land Surfaces Using Bistatically Scattered GNSS Signals from Low Earth Orbit. Doctoral Thesis. — Guildford : University of Surrey, 2006.

Gleason S. Towards Sea Ice Remote Sensing with Space Detected GPS Signals: Demonstration of Technical Feasibility and Initial Consistency Check Using Low Resolution Sea Ice Information // Remote Sensing. — 2010. — Vol. 2, no. 8. — P. 2017–2039. — https://doi.org/10.3390/rs2082017.

Gleason S., Hodgart S., Sun Y., et al. Detection and Processing of bistatically reflected GPS signals from low Earth orbit for the purpose of ocean remote sensing // IEEE Transactions on Geoscience and Remote Sensing. — 2005. — Vol. 43, no. 6. — P. 1229–1241. — https://doi.org/10.1109/tgrs.2005.845643.

Gleason S., Lowe S. and Zavorotny V. Remote sensing using bistatic GNSS reflections // GNSS Applications and Methods / ed. by S. Gleason and D. Gebre-Egziabher. — Norwood : Artech House, 2009. — P. 399–436.

Golden K. M., Cheney M., Ding K., et al. Forward electromagnetic scattering models for sea ice // IEEE Transactions on Geoscience and Remote Sensing. — 1998. — Vol. 36, no. 5. — P. 1655–1674. — https://doi.org/10.1109/36.718637.

Hall C. D. and Cordey R. A. Multistatic Scatterometry // International Geoscience and Remote Sensing Symposium, "Remote Sensing: Moving Toward the 21st Century". — IEEE, 1988. — P. 561–562. — https://doi.org/10.1109/igarss.1988.570200.

Hallikainen M. and Winebrenner D. P. The physical basis for sea ice remote sensing // Microwave Remote Sensing of Sea Ice / ed. by F. D. Carsey. — Washington : American Geophysical Union, 1992. — P. 29–46. — https://doi.org/10.1029/gm068p0029.

Hauser D., Tison C., Amiot T., et al. SWIM: The First Spaceborne Wave Scatterometer // IEEE Transactions on Geoscience and Remote Sensing. — 2017. — Vol. 55, no. 5. — P. 3000–3014. — https://doi.org/10.1109/tgrs.2017.2658672.

Hobiger T., Haas R. and Löfgren J. S. GLONASS-R: GNSS reflectometry with a Frequency Division Multiple Access-based satellite navigation system // Radio Science. — 2014. — Vol. 49, no. 4. — P. 271–282. — https://doi.org/10.1002/2013rs005359.

Hwang P. A. and Fois F. Surface roughness and breaking wave properties retrieved from polarimetric microwave radar backscattering // Journal of Geophysical Research: Oceans. — 2015. — Vol. 120, no. 5. — P. 3640–3657. — https://doi.org/10.1002/2015jc010782.

JAXA. GPM Data Utilization Handbook. Version 1.0. — Japan Aerospace Exploration Agency, 2014. — 92 p.

Karaev V., Panfilova M., Ryabkova M., et al. Remote Sensing of Sea Ice at Small Incidence Angles: Verification of Theoretical Models // 2021 IEEE International Geoscience and Remote Sensing Symposium IGARSS. — IEEE, 2021. — P. 5629–5632. — https://doi.org/10.1109/IGARSS47720.2021.9554163.

Karaev V., Titchenko Y., Panfilova M., et al. Application of the Doppler Spectrum of the Backscattering Microwave Signal for Monitoring of Ice Cover: A Theoretical View // Remote Sensing. — 2022a. — Vol. 14, no. 10. — P. 2331. — https://doi.org/10.3390/rs14102331.

Karaev V., Titchenko Y., Panfilova M., et al. On the Problem of the Sea Ice Detection by Orbital Microwave Doppler Radar at the Nadir Sounding // Remote Sensing. — 2022b. — Vol. 14, no. 19. — P. 4937. — https://doi.org/10.3390/rs14194937.

Karaev V., Titchenko Y., Panfilova M., et al. The Doppler Spectrum of the Microwave Radar Signal Backscattered From the Sea Surface in Terms of the Modified Bragg Scattering Model // IEEE Transactions on Geoscience and Remote Sensing. — 2020. — Vol. 58, no. 1. — P. 193–202. — https://doi.org/10.1109/tgrs.2019.2935343.

Kintner P. M., Ledvina B. M. and Paula E. R. de. GPS and ionospheric scintillations // Space Weather. — 2007. — Vol. 5, no. 9. — S09003. — https://doi.org/10.1029/2006sw000260.

Komarov A. S. and Buehner M. Detection of First-Year and Multi-Year Sea Ice from Dual-Polarization SAR Images Under Cold Conditions // IEEE Transactions on Geoscience and Remote Sensing. — 2019. — Vol. 57, no. 11. — P. 9109–9123. — https://doi.org/10.1109/tgrs.2019.2924868.

Komarov A. S., Isleifson D., Barber D. G., et al. Modeling and Measurement of C-Band Radar Backscatter From Snow-Covered First-Year Sea Ice // IEEE Transactions on Geoscience and Remote Sensing. — 2015. — Vol. 53, no. 7. — P. 4063–4078. — https://doi.org/10.1109/tgrs.2015.2390192.

Kovaldov D., Titchenko Y., Karaev V., et al. Method for Calculating the Dependence of the Backscattering Radar Cross Section for Freshwater Ice on the Incidence Angle Using the Doppler Spectrum // IGARSS 2024 - 2024 IEEE International Geoscience and Remote Sensing Symposium. — IEEE, 2024. — P. 107–110. — https://doi.org/10.1109/igarss53475.2024.10640985.

Kudryavtsev V. N., Makin V. K. and Chapron B. Coupled sea surface-atmosphere model: 2. Spectrum of short wind waves // Journal of Geophysical Research: Oceans. — 1999. — Vol. 104, no. C4. — P. 7625–7639. — https://doi.org/10.1029/1999jc900005.

Lagerloef G., Colomb F. C., Le Vine D., et al. The Aquarius/SAC-D Mission: Designed to Meet the Salinity Remote-Sensing Challenge // Oceanography. — 2008. — Vol. 21, no. 1. — P. 68–81. — https://doi.org/10.5670/oceanog.2008.68.

Larson K. M., Gutmann E. D., Zavorotny V. U., et al. Can we measure snow depth with GPS receivers? // Geophysical Research Letters. — 2009. — Vol. 36, no. 17. — P. L17502. — https://doi.org/10.1029/2009gl039430.

Lebedev G. A. and Sukhorukov K. K. Propagation of Electromagnetic and Acoustic Waves in Sea Ice. — Saint Petersburg : Russian State Hydrometeorological University, 2001. — 82 p. — EDN: RAXRWZ ; (in Russian).

Li C. and Huang W. An Algorithm for Sea-Surface Wind Field Retrieval From GNSS-R Delay-Doppler Map // IEEE Geoscience and Remote Sensing Letters. — 2014. — Vol. 11, no. 12. — P. 2110–2114. — https://doi.org/10.1109/lgrs.2014.2320852.

Lopatin V. P., Murzabekov M. M. and Bobrov D. S. Results of determining the geoid height profile and vertical line deviation using GNSS signals reflected from water surface // Geodesy and Cartography. — 2024. — Vol. 1004, no. 2. — P. 21–30. — https://doi.org/10.22389/0016-7126-2024-1004-2-21-30.

Lopatin Vladislav and Fateev Vyacheslav. Methods of Bistatic GNSS-Radio Altimetry for Determining Height Profile of the Ocean and Their Experimental Verification // 5th Symposium on Terrestrial Gravimetry: Static and Mobile Measurements (TG-SMM 2019). — Cham : Springer International Publishing, 2022. — P. 127–132. — https://doi.org/10.1007/1345_2022_139.

Mahmud M. S., Geldsetzer T., Howell S. E. L., et al. Incidence Angle Dependence of HH-Polarized C- and L-Band Wintertime Backscatter Over Arctic Sea Ice // IEEE Transactions on Geoscience and Remote Sensing. — 2018. — Vol. 56, no. 11. — P. 6686–6698. — https://doi.org/10.1109/tgrs.2018.2841343.

Martín-Neira M. A Passive Reflectometry and Interferometry System (PARIS): Application to ocean altimetry // ESA Journal. — 1993. — Vol. 17. — P. 331–355.

McMullan K. D., Brown M. A., Martín-Neira M., et al. SMOS: The Payload // IEEE Transactions on Geoscience and Remote Sensing. — 2008. — Vol. 46, no. 3. — P. 594–605. — https://doi.org/10.1109/tgrs.2007.914809.

Melsheimer C. and Spreen G. AMSR2 ASI sea ice concentration data, Antarctic, version 5.4 (NetCDF) (July 2012 - December 2019). — 2019. — https://doi.org/10.1594/PANGAEA.898400.

MERRByS. Measurement of Earth Reflected Radio-navigation signals By Satellite. — URL: https://merrbys.co.uk/ (visited on 08/20/2025).

Mitnik L. M. and Kalmykov A. I. Structure and dynamics of the Sea of Okhotsk marginal ice zone from "ocean" satellite radar sensing data // Journal of Geophysical Research: Oceans. — 1992. — Vol. 97, no. C5. — P. 7429–7445. — https://doi.org/10.1029/91jc01596.

Mitnik L. M. and Viktorov S. V. Radar Location of the Earth's Surface from Space. — Saint Petersburg : Gidrometeoizdat, 1990. — 200 p. — EDN: LTMGKT ; (in Russian).

Najibi N. and Jin S. Physical Reflectivity and Polarization Characteristics for Snow and Ice-Covered Surfaces Interacting with GPS Signals // Remote Sensing. — 2013. — Vol. 5, no. 8. — P. 4006–4030. — https://doi.org/10.3390/rs5084006.

Nogués-Correig O., Galí E. C., Campderrós J. S., et al. A GPS-Reflections Receiver That Computes Doppler/Delay Maps in Real Time // IEEE Transactions on Geoscience and Remote Sensing. — 2007. — Vol. 45, no. 1. — P. 156–174. — https://doi.org/10.1109/TGRS.2006.882257.

Onstott R. G. SAR and scatterometer signatures of sea ice // Microwave Remote Sensing of Sea Ice / ed. by F. D. Carsey. — Washington : American Geophysical Union, 1992. — P. 73–104. — https://doi.org/10.1029/gm068p0073.

Ryabkova M., Karaev V., Guo J., et al. A Review of Wave Spectrum Models as Applied to the Problem of Radar Probing of the Sea Surface // Journal of Geophysical Research: Oceans. — 2019. — Vol. 124, no. 10. — P. 7104–7134. — https://doi.org/10.1029/2018jc014804.

Sandven S., Spreen G., Heygster G., et al. Sea Ice Remote Sensing-Recent Developments in Methods and Climate Data Sets // Surveys in Geophysics. — 2023. — Vol. 44, no. 5. — P. 1653–1689. — https://doi.org/10.1007/s10712-023-09781-0.

Smith G. C., Allard R., Babin M., et al. Polar Ocean Observations: A Critical Gap in the Observing System and Its Effect on Environmental Predictions From Hours to a Season // Frontiers in Marine Science. — 2019. — Vol. 6. — https://doi.org/10.3389/fmars.2019.00429.

Sutton R., Schroeder E., Thompson A., et al. Satellite-Aircraft Multipath and Ranging Experiment Results at L Band // IEEE Transactions on Communications. — 1973. — Vol. 21, no. 5. — P. 639–647. — https://doi.org/10.1109/tcom.1973.1091693.

Timchenko A. I., Sinitsyn Y. A. and Efimov V. B. Simulation of radio wave scattering by ice coatings // Radiophysics and Quantum Electronics. — 1985. — Vol. 28, no. 7. — P. 556–561. — https://doi.org/10.1007/bf01034097.

Titchenko Y. Bistatic Doppler spectrum of radiation reflected by a water surface // Russian Journal of Earth Sciences. — 2020. — Vol. 20, no. 6. — ES6007. — https://doi.org/10.2205/2020es000745.

Ulaby F. T., Moore R. K. and Fung A. K. Microwave Remote Sensing. Vol. 3: From Theory to Applications. — Artech House, 1986.

Vagapov Z. K., Gavrilo V. P., Kozlov A. I., et al. Remote Sensing Methods for Sea Ice Research. — Saint Petersburg : Gidrometeoizdat, 1993. — 342 p. — EDN: ALWNAJ ; (in Russian).

Voronovich A. G. Small-slope approximation for electromagnetic wave scattering at a rough interface of two dielectric half-spaces // Waves in Random Media. — 1994. — Vol. 4, no. 3. — P. 337–367. — https://doi.org/10.1088/0959-7174/4/3/008.

Voronovich A. G. and Zavorotny V. U. Theoretical model for scattering of radar signals in Ku- and C-bands from a rough sea surface with breaking waves // Waves in Random Media. — 2001. — Vol. 11, no. 3. — P. 247–269. — https://doi.org/10.1080/13616670109409784.

Winebrenner D. P., Bredow J., Fung A. K., et al. Microwave sea ice signature modeling // Microwave Remote Sensing of Sea Ice / ed. by F. D. Carsey. — Washington : American Geophysical Union, 1992. — P. 137–175. — https://doi.org/10.1029/gm068p0137.

Yan Q. and Huang W. Sea Ice Sensing From GNSS-R Data Using Convolutional Neural Networks // IEEE Geoscience and Remote Sensing Letters. — 2018. — Vol. 15, no. 10. — P. 1510–1514. — https://doi.org/10.1109/lgrs.2018.2852143.

Yan Q. and Huang W. Sea Ice Remote Sensing Using GNSS-R: A Review // Remote Sensing. — 2019. — Vol. 11, no. 21. — P. 2565. — https://doi.org/10.3390/rs11212565.

Yan Q., Huang W. and Moloney C. Neural Networks Based Sea Ice Detection and Concentration Retrieval From GNSS-R Delay-Doppler Maps // IEEE Journal of Selected Topics in Applied Earth Observations and Remote Sensing. — 2017. — Vol. 10, no. 8. — P. 3789–3798. — https://doi.org/10.1109/jstars.2017.2689009.

Yang T., Wan W., Sun Z., et al. Comprehensive Evaluation of Using TechDemoSat-1 and CYGNSS Data to Estimate Soil Moisture over Mainland China // Remote Sensing. — 2020. — Vol. 12, no. 11. — P. 1699. — https://doi.org/10.3390/rs12111699.

Zapevalov A. S. and Knyazkov A. S. Simulation of characteristics of the sea surface for problems of quasi-specular reflection of radio waves // Processes in Geomedia. — 2019. — 4 (22). — P. 490–496. — EDN: GRBOQO ; (in Russian).

Zavorotny V. U., Gleason S., Cardellach E., et al. Tutorial on Remote Sensing Using GNSS Bistatic Radar of Opportunity // IEEE Geoscience and Remote Sensing Magazine. — 2014. — Vol. 2, no. 4. — P. 8–45. — https://doi.org/10.1109/mgrs.2014.2374220.

Zhu Y., Yu K., Zou J., et al. Sea Ice Detection Based on Differential Delay-Doppler Maps from UK TechDemoSat-1 // Sensors. — 2017. — Vol. 17, no. 7. — P. 1614. — https://doi.org/10.3390/s17071614.